# Earthquakes indicated magma viscosity during Kīlauea's 2018 eruption

https://doi.org/10.1038/s41586-021-03400-x

Received: 5 August 2020

Accepted: 26 February 2021

**D. C. Roman**[1]✉, **A. Soldati**[2], **D. B. Dingwell**[2], **B. F. Houghton**[3] & **B. R. Shiro**[4]

Magma viscosity strongly controls the style (for example, explosive versus effusive) of a volcanic eruption and thus its hazard potential, but can only be measured during or after an eruption. The identification of precursors indicative of magma viscosity would enable forecasting of the eruption style and the scale of associated hazards[1]. The unanticipated May 2018 rift intrusion and eruption of Kīlauea Volcano, Hawai'i[2] displayed exceptional chemical and thermal variability in erupted lavas, leading to unpredictable effusion rates and explosivity. Here, using an integrated analysis of seismicity and magma rheology, we show that the orientation of fault-plane solutions (which indicate a fault's orientation and sense of movement) for earthquakes preceding and accompanying the 2018 eruption indicate a 90-degree local stress-field rotation from background, a phenomenon previously observed only at high-viscosity eruptions[3], and never before at Kīlauea[4–8]. Experimentally obtained viscosities for 2018 products and earlier lavas from the Pu'u 'Ō'ō vents tightly constrain the viscosity threshold required for local stress-field reorientation. We argue that rotated fault-plane solutions in earthquake swarms at Kīlauea and other volcanoes worldwide provide an early indication that unrest involves magma of heightened viscosity, and thus real-time monitoring of the orientations of fault-plane solutions could provide critical information about the style of an impending eruption. Furthermore, our results provide insight into the fundamental nature of coupled failure and flow in complex multiphase systems.

Many volcanoes erupt lavas that are variable in composition, temperature and texture—and hence in bulk viscosity—in successive eruptions, and even within a single eruptive episode[9–14]. Lava viscosity influences how far and how fast a lava flow will travel[15], with more viscous lavas generally forming smaller, thicker lava flows or even lava coulées and domes. Higher viscosity also inhibits early degassing and outgassing, leading to overpressure and greater potential for a powerful explosive eruption[16]. Furthermore, the viscosity of basaltic magma may influence the number of fissures formed during an eruption, so that more viscous basalts tend to be erupted through numerous, short-lived fissures, as in the early phases of the 1955 and 2018 eruptions of Kīlauea Volcano, Hawai'i[2,17].

Combined, the phenomena described above clearly highlight the value of accurate pre-eruptive indicators of magma viscosity, especially for eruptions that may display substantial chemical and thermal variability, as in the 2018 Kīlauea eruption. At Kīlauea in 2018, rapid geochemical characterization was performed within hours of sample collection, and this provided critical information to scientists and emergency management officials about the potential for changing eruptive hazards[14]. However, the presence of low-temperature, differentiated lavas in the early phases of the eruption was only recognized after the eruption began. Identification of a geophysical proxy for magma viscosity that could be applied during precursory unrest would provide more time to develop mitigation strategies and anticipate upcoming changes in eruptive behaviour.

The 2018 lower East Rift Zone (LERZ) eruption of Kīlauea provides an unprecedented opportunity to test a hypothesized link between magma viscosity and the occurrence of an approximately 90° rotation of accompanying volcano-tectonic earthquake fault-plane solutions (FPS)[3]. For the first time, both FPS and rheological data are available for the same volcano for eruptions of high- and low-viscosity magma. Since 1983, Kīlauea has erupted only low-viscosity basalt, accompanied by earthquakes with non-rotated FPS. As 90° local stress-field rotations have previously been observed only in association with higher-bulk-viscosity eruptions, we hypothesize that a local stress-field rotation should have accompanied the displacement and eruption of more evolved and thus more viscous basaltic magma in the first month of the 2018 eruption.

Here we show that double-couple (that is, assuming no volumetric component of fault displacement) FPS for precursory and syneruptive volcano-tectonic earthquakes provided an indication of subsurface movement of more viscous magma during the precursory and early stages of the 2018 LERZ eruption. Near-real-time analysis of FPS orientations is thus a useful monitoring tool for anticipating eruptive behaviours modulated by magma viscosity. Furthermore, we show that an increase in magma viscosity of a factor of less than one order of magnitude, owing to changes in both magma composition and temperature, is a plausible driver of this key transition in the mechanism and character of volcano-tectonic seismicity.

---

[1]Earth and Planets Laboratory, Carnegie Institution for Science, Washington, DC, USA. [2]Ludwig-Maximilians-Universität München, Munich, Germany. [3]School of Ocean and Earth Science and Technology, University of Hawai'i at Mānoa, Honolulu, HI, USA. [4]USGS Hawaiian Volcano Observatory, United States Geological Survey, Hilo, HI, USA. ✉e-mail: droman@carnegiescience.edu

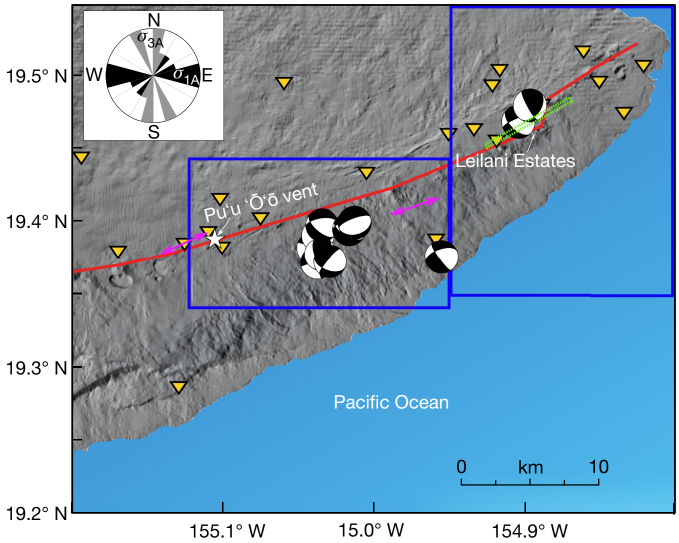

**Fig. 1 | Overview of Kīlauea Volcano, HV seismic network (inverted orange triangles), and locations/FPS showing fault orientation and sense of slip (beachball symbols) for 11 background-period earthquakes in LERZ.** The red line shows the approximate trend of the LERZ[23]. The green dashed box shows the location of 2018 eruption fissures (from ref. [2]). The magenta arrows show azimuth of fast split S-wavelets at stations STCD and HULD[24]. The blue boxes correspond to sub-areas (left is the upper LERZ, right is the lower LERZ). The white star indicates the Pu'u 'Ō'ō vent. The inset is a rose diagram of P- or T-axis azimuths (15° bins; black is the P-axis azimuth if the P dip is <45°, grey is the T-axis azimuth if the P dip is >45°). Inferred azimuths of $\sigma_{1A}$ and $\sigma_{3A}$ are indicated in the inset.

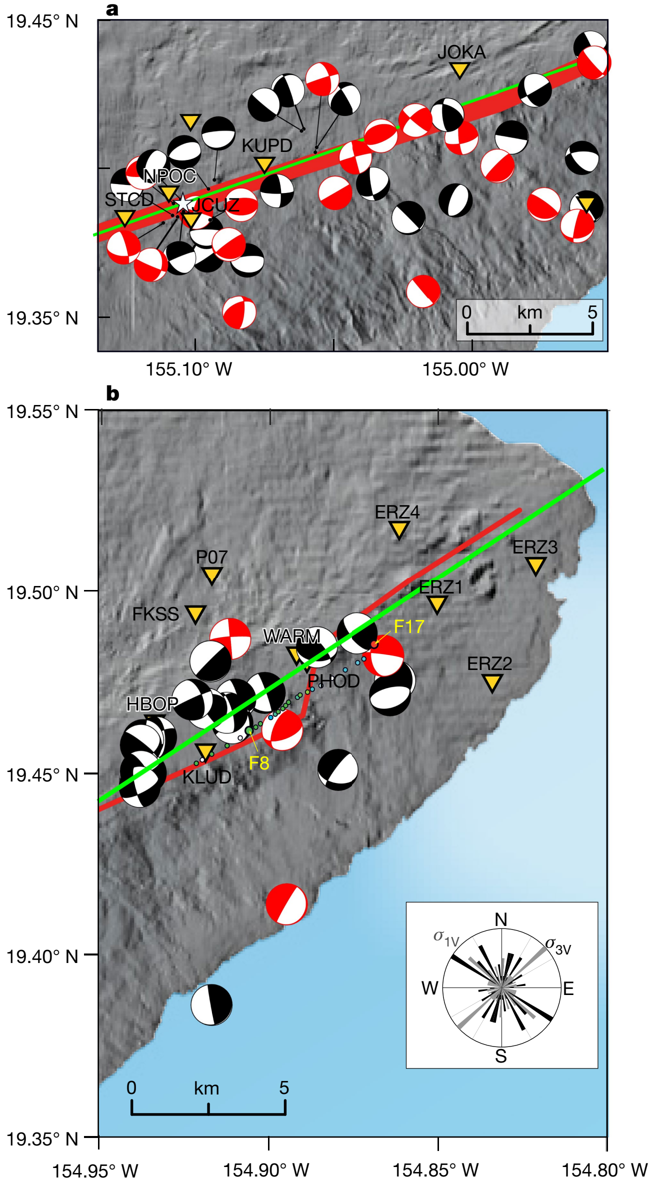

**Fig. 2 | Map views of eruption FPS. a**, upper LERZ; **b**, lower LERZ. Rotated FPS are shown as red beachballs and non-rotated FPS are shown as black beachballs —see Methods for a description of identification criteria. The star symbol in **a** marks the location of the Pu'u 'Ō'ō vent. The coloured dots in **b** mark the locations of 2018 fissures[2] (red (labelled F17), andesite end-member; green, high-Ti end-member; blue, mafic end-member; white, not reported[14]). The Fissure 8 and Fissure 17 locations are labelled F8 and F17 and indicated by large green and red dots, respectively. See Fig. 1 for map locations. The green lines indicate the location and strike of the dike used for Coulomb stress analysis (the red line shows the LERZ trend[23]). The inset in **b** shows a rose diagram of all P- or T-axis azimuths in **a** and **b** (5° bins; black shows the P-axis azimuth if the P dip is <45°, grey shows T-axis azimuths if the P dip is >45°). Inferred azimuths of $\sigma_{1V}$ and $\sigma_{3V}$ are indicated.

Rotations of the axis of local maximum compression ($\sigma_1$, proxied here by FPS P-axis orientations) by approximately 90° have been observed in double-couple FPS for volcano-tectonic earthquakes prior to and during eruptions[18,19], and have been linked to stresses produced in the walls of an inflating or pressurizing dike[20]. Such stress-field rotations of around 90° have been documented only in cases where the erupted magma is highly evolved and/or partially crystalline[3], and thus may reflect the magnitude of stress that is normal to the flow direction during magma emplacement. Dynamic normal stresses may result from a volume increase during flow of highly crystalline magma under a velocity gradient, via a nonlinear process known as shear dilatancy[21], from a high liquid viscosity (such as silica-rich melts), or through the addition of trapped bubbles to the melt by vesiculation accompanying decompression in a high-bulk-viscosity magma. Numerical modelling demonstrates that a strongly deviatoric ambient stress field (that is, where $\sigma_{1A} \gg \sigma_{3A}$) can suppress a local stress-field rotation during dike emplacement[22]. Therefore, comparison of local stress-field response at a single volcano between episodes of low- and high-viscosity magma transport is necessary to prove the hypothesized link between magma viscosity and stress-field rotation.

The 2018 rift eruption of Kīlauea[2] represented the first eruptive activity in the LERZ since the January–February 1960 Kapoho eruption[23]. Following a period of inflation at the long-lived Pu'u 'Ō'ō vent beginning in mid-March 2018 and culminating in a collapse of the Pu'u 'Ō'ō cone on 30 April 2018 (1 May 2018 Coordinated Universal Time, UTC), a swarm of volcano-tectonic earthquakes began on 1 May and migrated downrift as a dike propagated into the upper LERZ, as indicated by interferometric satellite radar (InSAR) and seismic data[2].The first of 24 eruptive fissures opened in the Leilani Estates subdivision (lower LERZ) on 4 May 2018 (UTC)[2]. Petrology[14] has been used to define four general eruptive phases on the main fissure system for subsequent activity through August 2018: Early Phase 1 (3–9 May 2018) involved 15 fissures in or near Leilani Estates that erupted evolved tholeiitic basalt with MgO < 5 weight per cent and containing 30–40% crystals. Early Phase 1 fissures were relatively short-lived, and up to six fissures were in eruption simultaneously. A pause in eruptive activity occurred from 9 to 11 May 2018, followed by Late Phase 1 activity from 12 to 18 May 2018. Late Phase 1 involved eruption of substantially less fractionated magmas, containing 25–30% crystals. Fissure 17 erupted andesite and basaltic andesite from 13 to 25 May 2018, and was offset from the main fissure system. Andesite was erupted from the western end of the fissure in spaced Strombolian

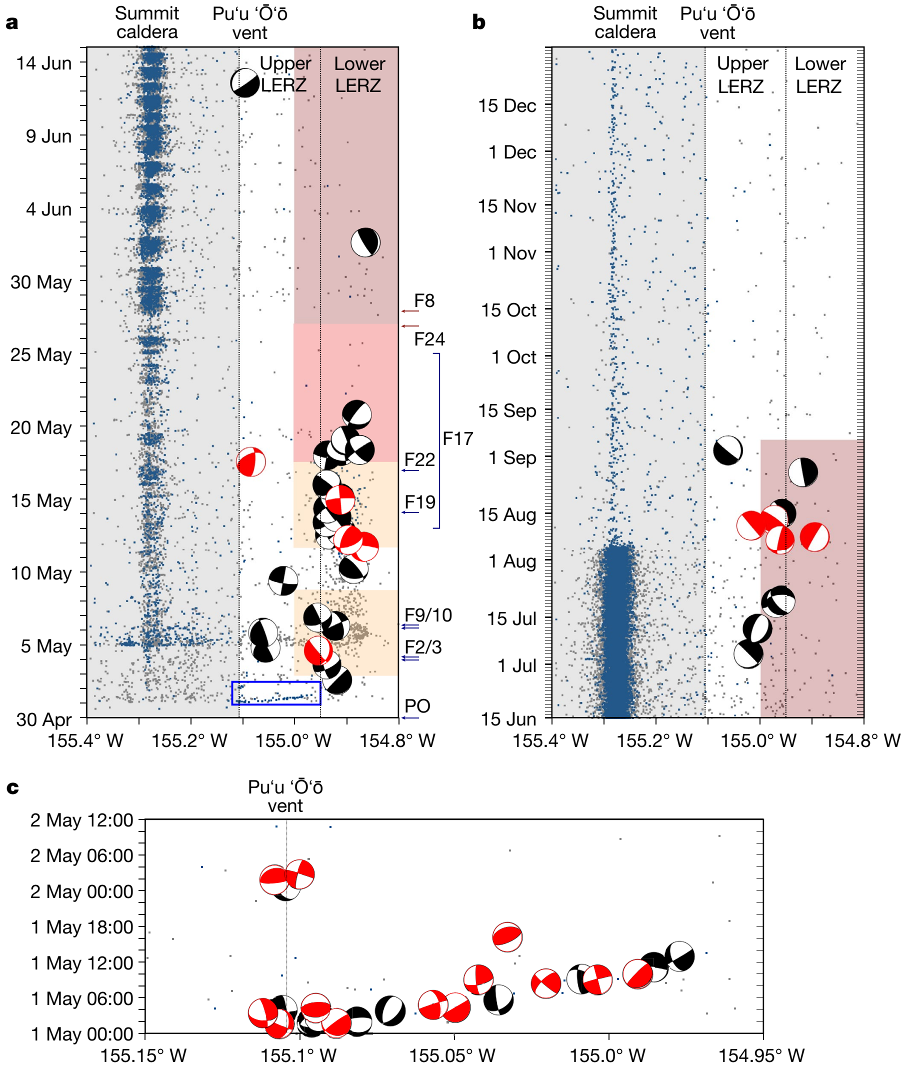

**Fig. 3 | Time–longitude plots of recorded earthquakes and FPS at Kīlauea Volcano during the study period. a**, 30 April to 15 June 2018; **b**, 15 June to 31 December 2018; **c**, 1 May 2018 00:00–12:00 (UTC). Blue dots indicate well located earthquakes; grey dots indicate other earthquakes. FPS with modelled positive Coulomb stress changes from dike inflation are shown as red beachballs, and FPS with modelled negative or zero Coulomb stress changes are shown as black beachballs. In **a**, the orange region indicates Phase 1 and the red region indicates Phase 2. In **a** and **b**, the maroon region indicates Phase 3. Arrows on the right edge of **a** mark the timing of fissures sampled for rheological analysis for each phase (Fig. 4). The blue box in **a** indicates the time and longitude range of **c**. Vertical dashed lines indicate the position of the Pu‘u ‘Ō‘ō vent and the longitude boundaries for the upper and lower LERZ. The grey region shows the seismicity uprift of Pu‘u ‘Ō‘ō vent.

explosions, whereas the eastern end discharged basaltic andesite in Hawaiian fountaining and rapid Strombolian explosions that fed a small lava flow. The onset of Phase 2 (17–27 May 2018) on the main fissure system was marked by a less dramatic change in lava chemistry to a more typical low-crystallinity basalt on the evening of 17 May 2018 at 19:26 local time[14], indicating that fresh magma had begun to erupt. Phase 3 is characterized by a massive outpouring of hot, relatively primitive basalt, which became focused on 28 May 2018 at Fissure 8, and continued with the progressive development of a lava pond confined within the Fissure 8 vent that persisted until 4 September 2018. Eruptive activity was more stable in June 2018 than in earlier phases, and the last substantial lava effusion (at Kīlauea's Fissure 8) was on 4 August 2018 (ref. [14]).

## Background FPS orientations in the LERZ

Whereas previous studies established that the ambient ($\sigma_A$) and syn-intrusion stress fields in the upper East Rift Zone (UERZ) and southwest Rift Zone (SWRZ) are characterized by a rift-parallel $\sigma_1$ during periods of quiescence and intrusion of low-viscosity basalt[4–8], the orientation of $\sigma_{1A}$ has not yet been established in the LERZ. Calculation of accurate background FPS is challenging in the LERZ because of the low levels of seismicity in this sector of the volcano, and the sub-optimal distribution of seismometers (mostly in a line along the rift zone). The fast wavelet polarization of split shear waves (a second proxy for the orientation of $\sigma_1$) from local earthquakes at Kīlauea from 2007 to 2014 at stations STCD (located just uprift of Pu‘u ‘Ō‘ō in the middle East Rift Zone (MERZ)) and HULD (located about 13 km downrift of Pu‘u ‘Ō‘ō in the LERZ, demobilized in 2012) is rift-parallel[24], consistent with a rift-parallel $\sigma_{1A}$ axis in the LERZ. We calculated 11 double-couple FPS for shallow earthquakes at Pu‘u ‘Ō‘ō and in the LERZ in 2016–2018 and 2019 (Fig. 1). We assume that LERZ FPS during these periods reflect background stresses, while Pu‘u ‘Ō‘ō FPS reflect stresses during transport and eruption of low-viscosity magma through the Pu‘u ‘Ō‘ō vent(s). These FPS have rift-parallel P-axes, confirming that $\sigma_A$ in the LERZ is characterized by a rift-parallel $\sigma_1$ axis, and that the stress field around Pu‘u ‘Ō‘ō is not rotated during eruption of low-viscosity basalt.

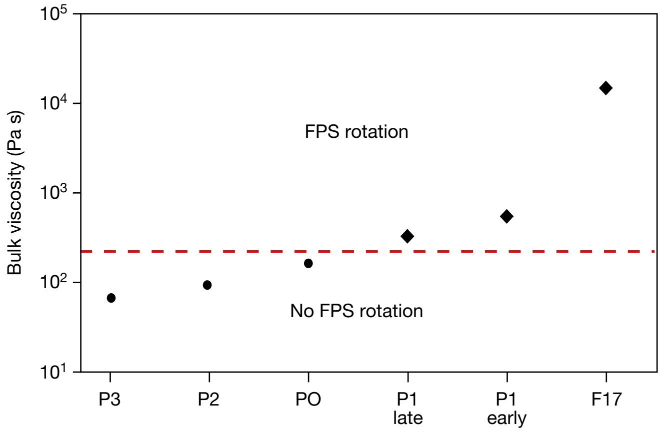

**Fig. 4 | Bulk viscosity of Kīlauea 2018 and Puʻu ʻŌʻō (PO) eruptive products.** Lower-viscosity (<~$10^2$ Pa s) magmas are not associated with periods of FPS rotation (circles), whereas higher-viscosity (>~$10^{2.5}$ Pa s) magmas are associated with periods of FPS rotation (diamonds). The red dashed line indicates the threshold bulk viscosity for FPS rotation. The *x* axis shows the phases; the timing and fissure number of samples for each phase are shown in Fig. 3.

## 2018 eruption FPS

We calculated 62 FPS for shallow (less than 4 km below sea level) earthquakes at Puʻu ʻŌʻō and in the LERZ from 1 May to 4 September 2018 (the LERZ eruption period) (Figs. 2, 3). In contrast to background FPS, eruption period FPS show two P-axis trends, one approximately rift-parallel, and another approximately rift-perpendicular (rotated approximately 90°). We classify 'rotated' FPS as those with a positive Coulomb stress change induced by an inflating rift-parallel dike. Earthquakes with rotated FPS are located in three areas: around Puʻu ʻŌʻō (7 out of 15 rotated, 47%), in the upper LERZ (11 out of 24 rotated, 46%), and in the lower LERZ (5 out of 23 rotated; 22%). These observations suggest that ~90°-rotated FPS may have been more prevalent around Puʻu ʻŌʻō and in the upper LERZ than in the lower LERZ. In the lower LERZ, we note that all of the ~90°-rotated FPS are located downrift of Fissure 8, where the eruption became focused at the beginning of Phase 3 (Fig. 2b).

The timing of rotated FPS in each area during Phases 1 and 2 generally corresponds to periods of locally high seismicity (Fig. 3). At Puʻu ʻŌʻō, rotated FPS occur from the onset of swarm propagation on 1 May 2018 to the end of Phase 1 on 17 May 2018. In the upper LERZ, rotated FPS occur on 1 and 4 May 2018 (early Phase 1), then again from 7 to 13 August 2018. In the lower LERZ, rotated FPS occur from 11 to 15 May 2018 (approximately late Phase 1 and onset of Fissure 17), and again on 8 August 2018 (Fig. 3). A magnitude $M_W = 6.9$ offshore earthquake on 4 May 2018 is also thought to have been triggered by dike intrusion[25]. This event would have resulted in increased tensile stresses perpendicular to the LERZ, perhaps accounting for the paucity of LERZ earthquakes with rotated FPS between 4 and 12 May 2018 (Fig. 3).

## Source location of evolved lavas

We interpret the overall stress-field rotation of about 90° as characterized by the orientation of volcano-tectonic FPS P-axes, as an indication of strong rift-perpendicular stresses generated during the failure of a barrier below Puʻu ʻŌʻō, propagation of a dike downrift through the LERZ, and early eruption phases (through Phase 1 into the beginning of Phase 2). Rift-perpendicular stresses, not expressed as an observable change in FPS orientation during previous episodes of basaltic dike intrusion at Kīlauea, are probably caused by shear dilatancy during subsurface flow of an atypically crystalline, evolved basalt through a system that contained stagnant pockets of more differentiated basaltic andesite and andesite that were emplaced during earlier LERZ activity decades to centuries prior to the 2018 episode[26–28]. Secondary evidence that volcano-tectonic earthquakes during the 2018 episode occurred in the walls of the propagating dike is apparent in the lateral spread of epicentres perpendicular to the dike (that is, epicentres do not form a tight line along the rift).

On the basis of our observations, we suggest that some of the magma transported through the UERZ to the Puʻu ʻŌʻō vent between 1983 and 2018 stagnated beneath Puʻu ʻŌʻō. Over time, these magmas partially crystallized, forming a semi-rigid barrier that impeded further transport downrift. The increase in summit magma pressures that manifested as a rise of the Halemaʻumaʻu lava lake and summit inflation beginning in mid-March 2018 (refs. [2,29]) also caused a pressure increase beneath Puʻu ʻŌʻō that culminated in the failure of the semi-rigid magma barrier, which was not expressed through an increase in seismicity beneath Puʻu ʻŌʻō owing to its ductile nature. Failure of this weak barrier on 1 May 2018 triggered the downrift transport of barrier magmas through a dike, which then encountered and mobilized additional higher-viscosity magma pockets in the LERZ and Leilani Estates area. Magmas sourced from some combination of stored evolved MERZ basalt and stagnant downrift magma pockets were injected downrift and erupted through Phase 1, followed in Phase 2 by additional low-viscosity magmas transported from uprift of Puʻu ʻŌʻō through a now-open (and thus largely aseismic) conduit system. By the end of the eruption, pressures throughout this open conduit system dropped to the point that the eruption at Fissure 8 could no longer be sustained. After the Fissure 8 vent shut down, a final reorganization of residual cool and crystal-rich magma occurred, leading to a final episode of FPS rotation.

## Viscosity threshold for FPS rotation

Experimentally determined liquid viscosities for Kīlauea 2018 samples range over three orders of magnitude (Fig. 4, Extended Data Table 1). Liquids from cool (about 1,110 °C; ref. [14]), early Phase 1 magma have viscosities of 188–228 Pa s at eruptive temperatures. This range decreased to 169–178 Pa s for late Phase 1. Liquid viscosities further dropped later in the eruption, to 70–93 Pa s during Phase 2 and 51–70 Pa s during Phase 3, as the eruptive temperatures rose to 1,180 °C (ref. [14]). Puʻu ʻŌʻō samples have a viscosity of 106 Pa s, intermediate between those for late Phase 1 and Phase 2 samples. Fissure 17 samples have a much higher and wider liquid viscosity range, between 550 Pa s and 9,770 Pa s. This is consistent with the much more evolved chemistry (basaltic andesite to andesite) as well as lower emplacement temperatures (1,062–1,098 °C; ref. [14]).

Liquid viscosities represent a lower limit for bulk magma viscosity, which is affected by the presence of crystals as well as by temperature and compositional variability. The crystal cargo for lavas from the main fissure system decreased as the eruption progressed[14], from 35% (by volume) during early Phase 1 to only 5% during Phase 3. Fissure 17, with the highest liquid viscosity, carried a 30–40% crystal cargo. Modelled bulk viscosities (Extended Data Table 1) are on the order of $10^2$ Pa s for magma emitted along the main fissure system in Phase 1, and $10^1$ Pa s for magma emitted along the main fissure system in Phases 2 and 3. Magma emitted at Fissure 17 has a much higher bulk viscosity of about $10^4$ Pa s, and Puʻu ʻŌʻō magma has a bulk viscosity of about $10^2$ Pa s.

We find that eruptive products whose viscosity is equal to or lower than $10^2$ Pa s (Phase 2 and Phase 3) are associated with a lack of FPS rotation (Fig. 4). Conversely, a viscosity equal to or higher than $10^{2.5}$ Pa s (Phase 1 evolved basalt and Fissure 17 basaltic andesite/basalt) is accompanied by FPS rotation. Thus, the bulk viscosity threshold for inducing stress-field rotation at Kīlauea is tightly constrained to one order of magnitude. Future work to determine the two-phase rheology of magmas from other eruptions with documented local stress-field responses through experimental work is thus critical to determine the universality of this viscosity threshold in relation to secondary factors such as differential ambient stress magnitude[22].

## Implications for forecasting

Our results demonstrate that the occurrence of ~90°-rotated FPS during and even after an episode of dike emplacement are indicative of the bulk viscosity of magma in the conduit. Thus, routine real-time calculation of volcano-tectonic FPS would complement other geophysical and geological methods for forecasting eruption hazards[30]. Optimization of seismic network configurations to allow robust FPS calculation (such as installation of additional stations off the rift axis) would help for future episodes at Kīlauea and elsewhere, where foreknowledge of the magma viscosity is important for anticipating and mitigating eruption hazards. We note that our observations from the period after the end of the Fissure 8 fountaining, in hindsight, were useful for tracking exactly what happened in the shallow conduit—after the end of surface discharge—specifically, the local sub-surface redistribution of high viscosity magma once the major throughput of hotter more primitive magma ended. Finally, we note that the establishment of a viscosity threshold for local stress-field rotation in volcanic systems will allow unambiguous assessment of the frequent earthquake swarms recorded at Earth's largest and most dangerous volcanoes, including Yellowstone[31], and whether they are driven by hydrothermal fluid circulation or by an episode of rhyolitic magma ascent[32].

## Online content

Any methods, additional references, Nature Research reporting summaries, source data, extended data, supplementary information, acknowledgements, peer review information; details of author contributions and competing interests; and statements of data and code availability are available at https://doi.org/10.1038/s41586-021-03400-x.

1. Sides, I. R., Edmonds, M., Maclennan, J., Swanson, D. A. & Houghton, B. F. Eruption style at Kīlauea Volcano in Hawai'i linked to primary melt composition. *Nat. Geosci*. **7**, 464–469 (2014).
2. Neal, C. A. et al. The 2018 rift eruption and summit collapse of Kilauea Volcano. *Science* **363**, 367–374 (2019).
3. Roman, D. C. & Cashman, K. V. The origin of volcano-tectonic earthquake swarms. *Geology* **34**, 457–460 (2006).
4. Karpin, T. L. & Thurber, C. H. The relationship between earthquake swarms and magma transport: Kilauea Volcano, Hawaii. *Pure Appl. Geophys*. **125**, 971–991 (1987).
5. Endo, E. T. Focal *Mechanisms for the May 15-18, 1970 Shallow Kilauea Earthquake Swarm*. Thesis, San Jose State College (1971).
6. Hill, D. P. A model for earthquake swarms. *J. Geophys. Res*. **82**, 1347–1352 (1977).
7. Lin, G. & Okubo, P. G. A large refined catalog of earthquake relocations and focal mechanisms for the Island of Hawai'i and its seismotectonic implications. *J. Geophys. Res*. **121**, 5031–5048 (2016).
8. Wauthier, C., Roman, D. C. & Poland, M. P. Modulation of seismic activity in Kīlauea's upper East Rift Zone (Hawai'i) by summit pressurization. *Geology* **47**, 820–824 (2019).
9. Hildreth, W., Fierstein, J., Champion, D. & Calvert, A. Mammoth Mountain and its mafic periphery—a late Quaternary volcanic field in eastern California. *Geosphere* **10**, 1315–1365 (2014).
10. Fierstein, J., Hildreth, W. & Calvert, A. T. Eruptive history of South Sister, Oregon Cascades. *J. Volcanol. Geotherm. Res*. **207**, 145–179 (2011).
11. Tarasewicz, J., White, R. S., Woods, A. W., Brandsdóttir, B. & Gudmundsson, M. T. Magma mobilization by downward-propagating decompression of the Eyjafjallajökull volcanic plumbing system. *Geophys. Res. Lett*. **39**, L19309 (2012).
12. Stock, M. et al. Cryptic evolved melts beneath monotonous basaltic shield volcanoes in the Galápagos Archipelago. *Nat. Commun*. **11**, 3767 (2020).
13. Ho, R. A. & Garcia, M. O. Origin of differentiated lavas at Kilauea Volcano, Hawaii: implications from the 1955 eruption. *Bull. Volcanol*. **50**, 35–46 (1988).
14. Gansecki, C. et al. The tangled tale of Kilauea's 2018 eruption as told by geochemical monitoring. *Science* **366**, eaaz0147 (2019).
15. Griffiths, R. W. The dynamics of lava flows. *Annu. Rev. Fluid Mech*. **32**, 477–518 (2000).
16. Cassidy, M., Manga, M., Cashman, K. V. & Bachmann, O. Controls on explosive-effusive volcanic eruption styles. *Nat. Commun*. **9**, 2839 (2018).
17. Macdonald, G. A. & Eaton, J. P. *Hawaiian Volcanoes During 1955*. USGS Bulletin 1171 https://doi.org/10.3133/b1171 (United States Geological Survey, 1964).
18. Roman, D. C. & Gardine, M. D. Seismological evidence for long-term and rapidly accelerating magma pressurization preceding the 2009 eruption of Redoubt Volcano, Alaska. *Earth Planet. Sci. Lett*. **371/372**, 226–234 (2013).
19. Lehto, H. L., Roman, D. C. & Moran, S. C. Temporal changes in stress preceding the 2004–2008 eruption of Mount St. Helens, Washington. *J. Volcanol. Geotherm. Res*. **198**, 129–142 (2010).
20. Roman, D. C. Numerical models of volcanotectonic earthquake triggering on non-ideally oriented faults. *Geophys. Res. Lett*. **32**, L02304 (2005).
21. Smith, J. V. Shear thickening dilatancy in crystal-rich flows. *J. Volcanol. Geotherm. Res*. **79**, 1–8 (1997).
22. Roman, D. C. & Heron, P. Effect of regional tectonic setting on local fault response to episodes of volcanic activity. *Geophys. Res. Lett*. **34**, L13310 (2007).
23. Wright, T. L. & Klein, F. W. *Two Hundred Years of Magma Transport and Storage at Kilauea Volcano, Hawai'i, 1790–2008*. USGS Professional Paper 1806 https://doi.org/10.3133/pp1806 (United States Geological Survey, 2014).
24. Johnson, J. H., Swanson, D. A., Roman, D. C., Poland, M. P. & Thelen, W. A. Crustal stress and structure at Kilauea Volcano inferred from seismic anisotropy. In *Hawaiian Volcanoes: From Source to Surface* (eds. Carey, R., Cayol, V., Poland, M. & Weis, D.) 251–268 (Wiley, 2015).
25. Chen, K. et al. Triggering of the MW 7.2 Hawaii earthquake of 4 May 2018 by a dike intrusion. *Geophys. Res. Lett*. **46**, 2503–2510 (2019).
26. Moore, R. B. Distribution of differentiated tholeiitic basalts on the lower east rift zone of Kilauea Volcano, Hawaii: a possible guide to geothermal exploration. *Geology* **11**, 136–140 (1983).
27. Lin, G., Shearer, P. M., Matoza, R. S., Okubo, P. G. & Amelung, F. Three-dimensional seismic velocity structure of Mauna Loa and Kilauea volcanoes in Hawaii from local seismic tomography. *J. Geophys. Res*. **119**, 4377–4392 (2014).
28. Teplow, W. et al. Dacite melt at the Puna geothermal venture wellfield, *Big Island of Hawaii. Trans. Geotherm. Resour. Council* **33**, 989–994 (2009).
29. Olivier, G., Brenguier, F., Carey, R., Okubo, P. & Donaldson, C. Decrease in seismic velocity observed prior to the 2018 eruption of Kilauea Volcano with ambient seismic noise interferometry. *Geophys. Res. Lett*. **46**, 3734–3744 (2019).
30. Patrick, M. R. et al. The cascading origin of the 2018 Kilauea eruption and implications for future forecasting. *Nat. Commun*. **11**, 5646 (2020).
31. Wicks, C. W., Thatcher, W., Dzurisin, D. & Svarc, J. Uplift, thermal unrest and magma intrusion at Yellowstone caldera. *Nature* **440**, 72–75 (2006).
32. Castro, J. M. & Dingwell, D. B. Rapid ascent of rhyolitic magma at Chaiten volcano, Chile. *Nature* **461**, 780–783 (2009).

# Methods

## Seismic analysis

For all volcano-tectonic earthquakes between 1 January 2014 and 31 January 2020 with a United States Geological Survey (USGS) Hawaiian Volcano Observatory (HVO) catalogue[33] location at or downrift of Puʻu ʻŌʻō (east of 155.125° W, and between 19.35° N and 19.55° N), a catalogue magnitude greater than 1.0, a catalogue depth above 4 km below sea level, and a catalogue azimuthal gap <180° (587 earthquakes), we repicked P-wave first-motion polarities (when a minimum of seven could be identified clearly) and combined our polarity picks with the HVO catalogue location for the event. For a period (18 May 2018 to 6 October 2018) when temporary seismic networks were deployed on- and off-shore (network Z6[34]: 9 July 2018 to 16 September 2018 and network 4S[35]: 27 July 2018 to 31 December 2018), we attempted to use picks from these stations to relocate (using HYP[36] and the standard/HVO velocity model for Kīlauea[37]) seismic events with catalogue azimuthal gaps >180° (159 additional earthquakes), and were able to produce new locations with azimuthal gap <180° for some of these events. In these cases, first-motion picks were combined with our relocation for FPS calculations. FPS were calculated using FPFIT[38] and evaluated for quality and rejected if they did not meet all of the following criteria: unique or similar multiple solutions, misfit of no more than 15% of the P-wave polarities, uncertainty in strike, dip and rake of ≤25°, and pressure ($P$)– and tension ($T$)–axis 95% confidence regions that cover ≤25% of the focal sphere. FPS that met these quality criteria have an average of 12 first-motion polarities, a maximum of 32 first-motion polarities, and a minimum of 7 first-motion polarities.

## Coulomb stress modelling

Using Coulomb 3.3[39,40], we calculate Coulomb stress changes induced by a dike striking N70°E (west of 154.95° W) or N57°E (east of 154.95° W) and opening by 1 metre. To exclude possible dike tip stresses, the model dike is infinitely long and infinitely tall. We assessed the resulting Coulomb stress change on both nodal planes and classified FPS as 'rotated' if either nodal plane experienced a positive Coulomb stress change. We calculate static Coulomb stress changes for individual earthquakes in each period based on their catalogue location (or our relocation for events with picks from networks Z6 or 4S), and fault orientation and sense of slip as indicated by our newly calculated FPS. All calculations are made in a homogeneous linearly elastic half-space with typical elastic parameters including a shear modulus of $5.0 \times 10^4$ MPa, Poisson's ratio of 0.25, and an effective coefficient of internal friction of 0.4.

## Sampling

Samples analysed for viscosity were collected from vents representative of all 2018 LERZ eruption phases, as well as from Puʻu ʻŌʻō. Samples are tephra, collected from along the fissure system during or shortly after the eruption. A sample of the very last material to be erupted from Puʻu ʻŌʻō (on 30 April) was collected on 4 May 2018. F8W is a small subsidiary feature just beyond the main Fissure 8 cone. Along Fissure 17, nine separate vents were sampled (A–I).

## Viscosity methods

The viscosity of magmatic melts depends on both temperature ($T$) and composition ($X$). Empirical viscosity models[41] can be used to predict silicate liquid viscosities as a function of both those parameters, but a residual mismatch persists between natural and modelled viscosities. Therefore, direct experimental measurements remain critical to assess the viscosity of magmatic liquids accurately. We performed such experimental measurements in a concentric cylinder rheometer[42]. In this apparatus, the rock sample is held in a platinum/rhodium crucible placed within a furnace, which re-melts it. A platinum/rhodium spindle is then inserted within the crucible and rotated at a controlled rate whereby the strain rate is imposed, and the stress is measured. From these two parameters, Newtonian viscosity of the pure liquid is calculated as the ratio of stress to strain rate. Instrumental accuracy is guaranteed by comparison of our results with international viscosity standard glasses.

Magmas are multi-phase materials, containing rigid inclusions of one or more crystalline phases, and/or rigid or deformable gas bubbles. Whereas pure silicate liquids are Newtonian ($\sigma = \eta\dot{\gamma}$, where $\sigma$ is the stress, $\eta$ is viscosity, and $\dot{\gamma}$ is the strain rate), crystal-bearing magmas and crystal-bearing plus bubble-bearing magmas exhibit complex rheological behaviour (see ref. [43] for a detailed review). The rheology of subliquidus, two-phase (melt and crystals) magma can be directly measured in the laboratory through high-temperature rheometry, but magmas with high crystal fraction are not tractable using these methods. Further, the effect of bubbles on magma viscosity remains difficult to evaluate in high-temperature laboratory measurements (especially for low-viscosity magmas such as basalts, where the timescales of bubble rise and relaxation are much shorter than experimental timescales) and must be modelled instead[43]. Here, we rely therefore on models[44] for suspension rheology effects to account for the effect of low-to-high crystal fractions on bulk magma viscosity with a consistent methodology, using crystallinity data from refs. [14,45]. The effect of bubbles is not considered, because the data necessary to do so (both bubble fraction and size relative to crystals) is not available for the dataset considered. Future work is necessary to fully assess the effect of bubbles on magma viscosity, as well as the extent to which variable vesiculation and crystallinity generate stresses normal to the flow at variable flow rates. However, regarding the latter, we anticipate that, particularly in relatively volatile-poor basaltic magmas flowing laterally, the effect will be minor.

# Data availability

Continuous seismic waveform data (network codes HV (https://doi.org/10.7914/SN/HV), Z6 (https://doi.org/10.7914/SN/Z6_2018), and 4S (https://doi.org/10.7914/SN/4S_2018) are available through the IRIS Data Management Center. A catalogue of located earthquakes is available through the USGS National Earthquake Information Center (https://doi.org/10.5066/F7MS3QZH). Source data are provided with this paper.

33. *Hawaiian Volcano Observatory Network* https://doi.org/10.7914/SN/HV (USGS Hawaiian Volcano Observatory, International Federation of Digital Seismograph Networks, 1956).
34. Wei, X., Shen, Y., Caplan-Auerbach, J. & Morgan, J. K. An OBS array to investigate offshore seismicity during the 2018 Kilauea eruption. *Seismol. Res. Lett.* **92**, 603–612 (2021).
35. Johnson, J. *UEA STAK Project* https://doi.org/10.7914/SN/4S_2018 (National Geoscience Data Centre, International Federation of Digital Seismograph Networks, 2018).
36. Lienert, B. R. & Havskov, J. A computer program for locating earthquakes both locally and globally. *Seismol. Res. Lett.* **66**, 26–36 (1995).
37. Klein, F. W. A linear gradient crustal model for south Hawaii. *Bull. Seismol. Soc. Am.* **71**, 1503–1510 (1981).
38. Reasenberg, P. & Oppenheimer, D. *FPFIT, FPPLOT and FPPAGE: FORTRAN Computer Programs for Calculating and Displaying Earthquake Fault Plane Solutions*. Open-File Report 85-739 https://doi.org/10.3133/ofr85739 (USGS, 1985).
39. Lin, J. & Stein, R. S. Stress triggering in thrust and subduction earthquakes and stress interaction between the southern San Andreas and nearby thrust and strike-slip faults. *J. Geophys. Res.* **109**, B02303 (2004).
40. Toda, S., Stein, R. S., Richards-Dinger, K. & Bozkurt, S. B. Forecasting the evolution of seismicity in southern California: animations built on earthquake stress transfer. *J. Geophys. Res.* **110**, B05S16 (2005).
41. Giordano, D., Russell, J. K. & Dingwell, D. B. Viscosity of magmatic liquids: a model. *Earth Planet. Sci. Lett.* **271**, 123–134 (2008).
42. Dingwell, D. B. & Virgo, D. The effect of oxidation state on the viscosity of melts in the system $Na_2O$-FeO-$Fe_2O_3$-$SiO_2$. *Geochim. Cosmochim. Acta* **51**, 195–205 (1987).
43. Mader, H. M., Llewellin, E. W. & Mueller, S. P. The rheology of two-phase magmas: a review and analysis. *J. Volcanol. Geotherm. Res.* **257**, 135–158 (2013).
44. Phan-Thien, N. & Pham, D. C. Differential multiphase models for polydispersed suspensions and particulate solids. *J. Non-Newt. Fluid Mech.* **72**, 305–318 (1997).
45. Chevrel, M. O. et al. The viscosity of pāhoehoe lava: in situ syn-eruptive measurements from Kilauea, Hawaii. *Earth Planet. Sci. Lett.* **493**, 161–171 (2018).

**Acknowledgements** We thank H. Dietterich, F. Pollitz, and F. Sigmundsson for constructive comments that improved the quality of this manuscript. A.S. acknowledges the support of the Alexander von Humboldt Postdoctoral Fellowship. D.B.D. was supported by ERC 2018 ADV

Grant 834225 (EAVESDROP). B.F.H. acknowledges funding by NSF EAR 1829188 and USGS Disaster Supplemental Research funding.

**Author contributions** D.C.R. and B.R.S. calculated earthquake locations and FPS. D.C.R. conducted Coulomb stress modelling. A.S. and D.B.D. conducted viscosity experiments and modelling. B.F.H. conducted sample collection. D.C.R. led the interpretation and writing of the manuscript, and all co-authors contributed to the interpretation and writing of the manuscript.

**Competing interests** The authors declare no competing interests.

**Additional information**
**Correspondence and requests for materials** should be addressed to D.C.R.
**Peer review information** *Nature* thanks Fred Pollitz and Freysteinn Sigmundsson for their contribution to the peer review of this work.
**Reprints and permissions information** is available at http://www.nature.com/reprints.

**Extended Data Table 1 | Experimentally determined and modelled viscosities for Kīlauea 2018 and Puʻu ʻŌʻō samples**

| Sample Location | F2, 3, 9, 10 | F19, 22 | F24 | F8, 8w | F17 (A-I) | Puʻu ʻŌʻō |
|---|---|---|---|---|---|---|
| Phase | P1 Early | P1 Late | P2 | P3 | Fissure 17 | - |
| Liquid Viscosity (Pa S) | 188 | 174 | 82 | 61 | 5160 | 106 |
| Crystal Fraction | 0.35 | 0.23 | 0.05 | 0.05 | 0.35 | 0.15 |
| Relative Viscosity | 2.94 | 1.92 | 1.14 | 1.14 | 2.94 | 1.50 |
| Bulk Viscosity (Pa S) | 5.5 x $10^2$ | 3.3 x $10^2$ | 9.3 x $10^1$ | 6.9 x $10^1$ | 1.5 x $10^4$ | 1.6 x $10^2$ |

Crystallinities and representative compositions for each phase may be found in refs. [14] and [44]. P indicates phase and F indicates fissure.